

Curvature-Specific Coupling Electrode Design for a Stretchable Three-Dimensional Inorganic Piezoelectric Nanogenerator

Junwoo Yea,[#] Jeongdae Ha,[#] Kyung Seob Lim, Hyeokjun Lee, Saehyuck Oh, Janghwan Jekal, Tae Sang Yu, Han Hee Jung, Jang-Ung Park, Taeyoon Lee, Jae-Woong Jeong, Hoe Joon Kim, Hohyun Keum, Yoon Kyeung Lee,^{*} and Kyung-In Jang^{*}



Cite This: *ACS Nano* 2024, 18, 34096–34106



Read Online

ACCESS |



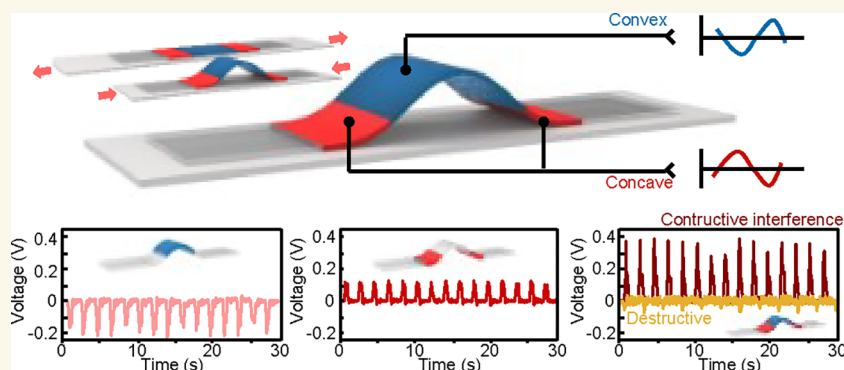
Metrics & More



Article Recommendations



Supporting Information



ABSTRACT: Structures such as 3D buckling have been widely used to impart stretchability to devices. However, these structures have limitations when applied to piezoelectric devices due to the uneven distribution of internal strain during deformation. When strains with opposite directions simultaneously affect piezoelectric materials, the electric output can decrease due to cancellation. Here, we report an electrode design tailored to the direction of strain and a circuit configuration that prevents electric output cancellation. These designs not only provide stretchability to piezoelectric nanogenerators (PENGs) but also effectively minimize electric output loss, achieving stretchable PENGs with minimal energy loss. These improvements were demonstrated using an inorganic piezoelectric material (PZT thin film) with a high piezoelectric coefficient, achieving a substantial maximum output power of $8.34 \text{ mW}/\text{cm}^3$. Theoretical modeling of the coupling between mechanical and electrical properties demonstrates the dynamics of energy harvesting, emphasizing the electrode design. In vitro and in vivo experiments validate the device's effectiveness in biomechanical energy harvesting. These results represent a significant advancement in stretchable PENGs, offering robust and efficient solutions for wearable electronics and biomedical devices.

KEYWORDS: piezoelectric nanogenerators, stretchable electronics, inorganic, 3D structure, energy harvesting

Piezoelectric nanogenerators (PENGs) are utilized across various engineering fields. PENG devices are extensively adopted in applications such as wearable,^{1,2} implantable,^{3–10} structural monitoring,^{11–14} and environmental^{15–18} due to their ability to harvest energy from natural movements to power electronic components. This capability is particularly advantageous in scenarios where battery replacement is challenging or when a continuous, low-power supply is essential. In the early stages of PENG research, cantilever-shaped inorganic piezoelectric devices were extensively studied, enabling efficient energy harvesting from high-

frequency vibration.^{11,19–27} However, these conventional designs are limited when they are applied to flexible and stretchable formats.

Received: July 23, 2024

Revised: November 11, 2024

Accepted: November 21, 2024

Published: December 5, 2024



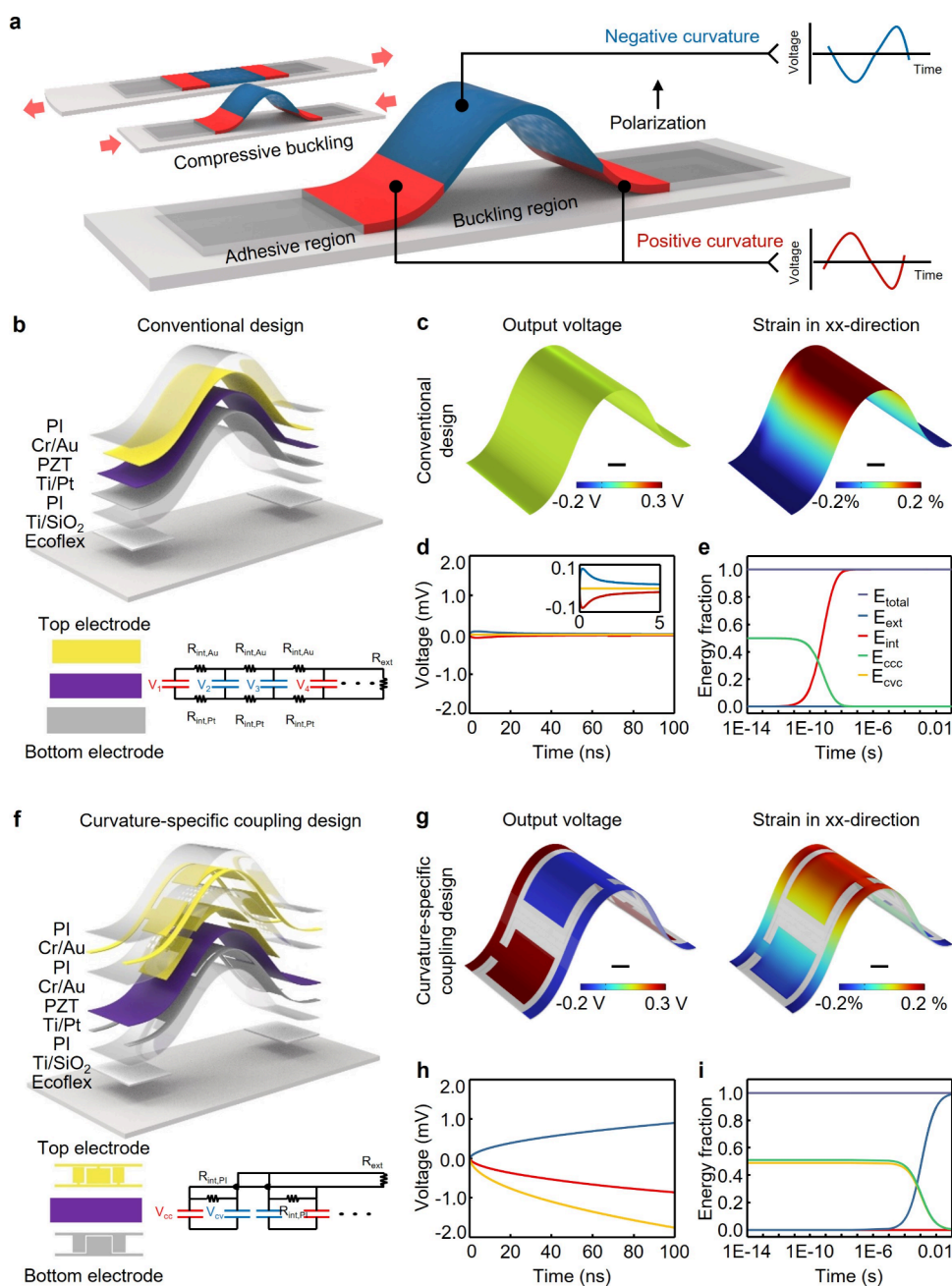


Figure 1. Principle and design of the S-PENG with curvature-specific electrodes. (a) Structure of the S-PENG. Compressive buckling induces regions with positive (red) and negative (blue) curvatures, generating opposite local polarity across the PZT layer in response to strain. (b) Representation of the conventional electrode design that electrically coupled regions with different curvatures. (c) Finite element analysis (FEA) for the 3D PZT nanogenerator with conventional electrodes, showing output voltage and strain after compressive buckling. Scale bars, 100 μm . (d) Output voltage and (e) electrical energy fraction generated during elongation with a strain rate of 90% per second. (f) Illustration of the curvature-specific electrode design. (g–i) Output voltage and strain (g), output voltage (h), and electrical energy fraction (i) of the device with curvature-specific electrodes, respectively.

There have been ongoing efforts to develop stretchable PENGs (S-PENGs), which can be categorized into two approaches: using polymer-based piezoelectric materials^{28–30} or employing strain-insensitive structures (e.g., serpentine,^{31,32} 3D buckling,^{33–35} and kirigami^{29,36,37}). Polymer-based piezoelectric materials, such as polyvinylidene fluoride (PVDF) and copolymers like poly(vinylidene fluoride–trifluoroethylene) (P(VDF–TrFE)), offer a high mechanical stretchability ($\sim 2\%$) and low stiffness (~ 2.5 GPa), thereby broadening the potential applications of S-PENGs.³⁸ However, their piezo-

electric coefficient is more than 10 times lower than those of ceramic-based piezoelectric materials, leading to significantly reduced output power.³⁹ To enhance the performance of organic polymer-based S-PENGs, organic–inorganic hybrid materials have been developed.^{39–42} While these composite-based S-PENGs have demonstrated improved energy efficiency over polymer-based PENGs, they exhibit a low piezoelectric coefficient and electric output.^{5,43} (Table S1)

Conversely, various studies have investigated the use of strain-insensitive structures in piezoelectric materials as a

promising approach for developing S-PENGs.^{29,31–37,41} The pioneering studies in this field demonstrated the potential of inorganic ceramic-based S-PENGs by imparting stretchability (~8%) to buckled PZT films.³⁴ However, the 3D buckling structure simultaneously generates local internal strains in opposite directions within the PZT, significantly reducing the electrical output. Not only buckling structures but also most strain-insensitive designs induce uneven local strain distributions, resulting in electrical output cancellation and considerable energy loss. Due to these structural limitations, despite the high piezoelectric coefficients and potential of inorganic piezoelectric materials, the integration of strain-insensitive structures with inorganic-based S-PENGs has not been successfully achieved. Similarly, despite recent efforts to design S-PENGs using organic piezoelectric materials combined with strain-insensitive structures, the issues of low piezoelectric coefficients and energy loss have not been resolved.^{29,31,32,36,37,41}

In this study, we report an approach that imparts stretchability to inorganic piezoelectric materials while minimizing energy loss through a curvature-specific coupling electrode design tailored for strain-insensitive structures (i.e., 3D buckling). To prevent the opposing local strains in the buckled PZT from canceling out the electrical output, the electrodes were divided into convex and concave regions according to the direction of the induced output voltage. Additionally, electrodes with outputs in the same direction were connected in parallel, whereas those with outputs in opposite directions were connected in series. This electrode design and circuit configuration ensure that the induced electrical energy is effectively used in the external load. To validate the effectiveness of this approach, theoretical and numerical analyses were conducted, demonstrating that the predicted electrical output of the S-PENGs closely matched the experimentally measured values. We show that this S-PENG achieves a power density of 8.34 mW/cm³, higher than those of conventional stretchable PENGs. The performance was further confirmed through wearable applications and in vivo energy harvesting from a porcine heart.

RESULTS AND DISCUSSION

Principle and Design of the S-PENG. The S-PENG is realized through the compressive buckling of planar devices, addressing the inherent challenges posed by the material's limited elastic modulus and maximum tensile strain. This approach incorporates 3D structures featuring wavy piezoelectric ribbons that partially detach from elastomeric substrates. The structure is induced by locally bonding flat PZT thin films to prestrained substrates. As the prestrain is released, the unrestrained regions (buckling regions) of the PZT thin film buckle upward (Figure 1a). By exploiting the buckled PZT layers, the global strain of the device is converted into flattening of the curvature, thereby mitigating strain within the thin PZT film. The precise control over the 3D buckling shape, including wavelength and amplitude, is achieved through the extent of prestrain of the substrate and other design parameters such as the location of bonding sites between the device and prestrained substrates.^{44–47}

The electrical polarity induced by the deformation of the PZT surface during stretching motion is governed by the strain exerted on the local region. When the neutral plane of the S-PENG is positioned beneath the PZT layer, the areas with negative curvature (convex regions) near the apex of the

curved configuration (blue region in Figure 1a) experience tensile strain, whereas the areas with positive curvature (concave regions) near the trough anchored to the substrate endure compressive strain (red region in Figure 1a). The difference in the local strain causes the output voltage in the opposite direction when the device is subject to mechanical deformation.

Conventional PENGs operating in the d31 mode induce an electric field perpendicular to the direction of the mechanical stress.^{27,33,48,49} These devices typically utilize a sandwich structure with two electrodes covering either the top or the bottom sides of the PZT layer (Figure 1b). However, the conventional design's electrical connection between regions with opposite curvatures significantly undermines the energy efficiency. The equivalent circuit model shown in the bottom diagram of Figure 1b elucidates the diminished output voltage of these nanogenerators. The piezoelectric layer with varying curvatures within one buckling period was modeled as four capacitors connected in parallel. These capacitors are directly interconnected through the Au and Pt, which induces immediate internal current flow between the capacitors with opposite curvature during stretching motion. This internal current lasts until it invalidates the vertical voltage difference of the PZT layer and dissipates the capacitive energy in each region (E_{CCC} and E_{CVC}) into Joule heating energy (E_{in}) through the internal resistance.

Figure 1c depicts the finite element analysis (FEA) simulation results of the strain in the xx direction (ϵ_{11}) in the buckling structure after the release of prestrain of the substrate to estimate the output voltage. Despite the locally nonzero deformation in the xx direction, the average value is zero, and the temporal output voltage essentially approaches zero. Figure 1d illustrates the output voltage during the more realistic scenario of elongation of the device with a strain rate of 90% per second. The analytical solution (Supporting Note 1) for the output voltage demonstrates the decay of output voltage of convex (blue) and concave (red) regions within approximately 10 ns due to the internal current. The electrical energy fraction over time, summarized in Figure 1e, shows that conventional electrodes dissipate the generated total electrical energy (E_{tot}) as Joule heating (E_{in}) due to internal current, rather than harvesting it through external load (E_{ext}) elements.

In contrast, Figure 1f introduces a segmented electrode structure based on their corresponding curvature. Unlike conventional electrode designs, our approach involves precisely patterning electrodes segmented within regions that share the same curvature. Subsequently, these curvature-specific coupling electrodes are connected at their terminals in a series configuration, effectively consolidating regions with the same curvature (polarity) and interconnecting regions with opposite polarities in series. The equivalent circuit model in the bottom of Figure 1f demonstrates electrical insulation between electrodes with different curvatures in principle due to the large resistance across polyimide gap, resulting in the dominant current flow through the external load. By connecting the capacitors with opposite curvature in series, the averaging out of the total output voltages is prevented. Figure 1g shows the simulation results for the strain and output voltage. While the strain level shows little difference, depending on the electrode design, the output voltage is clearly distinguishable. The analytical solution results for the transient dynamics of the voltage generated in the S-PENG with the curvature-specific coupling electrodes design are demonstrated in Figure 1h.

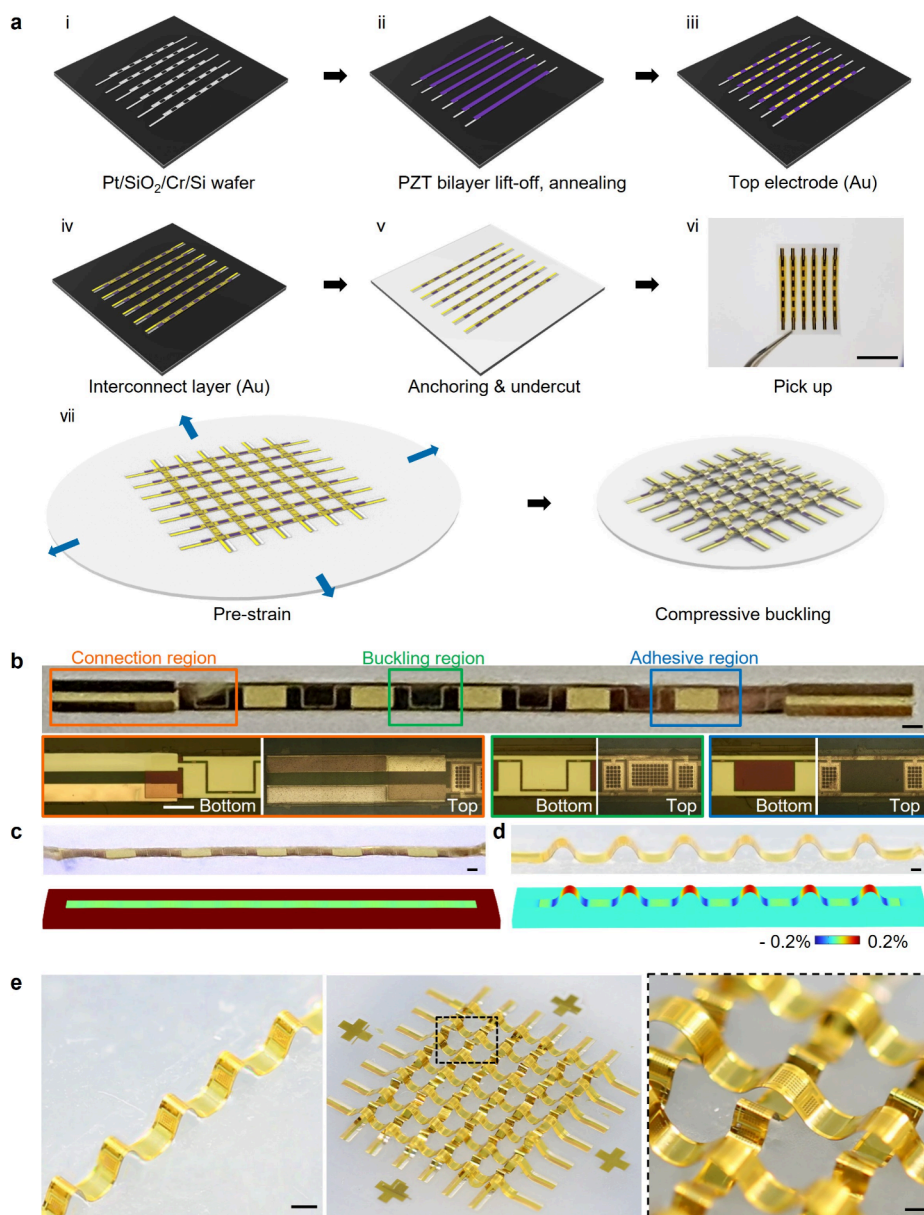


Figure 2. Fabrication process of the S-PENG. (a) Schematic illustration of the fabrication process for the S-PENG. Scale bars, 1 cm. (b–d) Optical images of the device on PI after the first transfer printing (b) and on the strained (c) or sequentially released (d) Ecoflex after the second transfer printing. (e) Optical images of the uni- and biaxially stretchable 3D PZT nanogenerators with curvature-specific coupling electrodes. Scale bars: 500 μm .

Unlike the conventional S-PENG, where the local output voltage decays rapidly, the proposed S-PENG design inhibits the decay of the output voltage in the convex (blue) and concave (red) regions. This is achieved by preventing internal current through the separated electrode design. Additionally, the serial connection between regions with opposite curvature results in the total output voltage being twice the magnitude of the local output voltage. This increase in the output voltage leads to improved energy efficiency. Unlike the conventional design, where energy waste due to internal current was dominant, the curvature-specific coupling electrode design allows all the electrical energy generated in the S-PENG to be utilized by the external load (Figure 1i).

Fabrication Process. The implementation of the curvature-specific coupling electrode design requires a fabrication technique capable of controlling local curvature in a

predetermined manner while remaining compatible with planar photolithography for electrode segmentation and global interconnection. Compressive buckling based on residual-stress-induced bending addresses these requirements effectively. Figure 2a illustrates the fabrication process for an S-PENG with curvature-specific electrodes. A two-step transferring process was developed, first from the wafer to a polyimide (PI) layer and then from the PI layer to a prestrained elastomeric substrate. This process accommodates the high-temperature annealing process of PZT, protects it from process chemicals, and forms bonding sites to the substrate for a controlled buckling structure.

The process begins with a bare silicon wafer serving as a temporary substrate. Before the bottom electrode is deposited, a double-layer stack of Cr and SiO₂ is deposited. The Cr layer maintains mechanical stability during the high-temperature

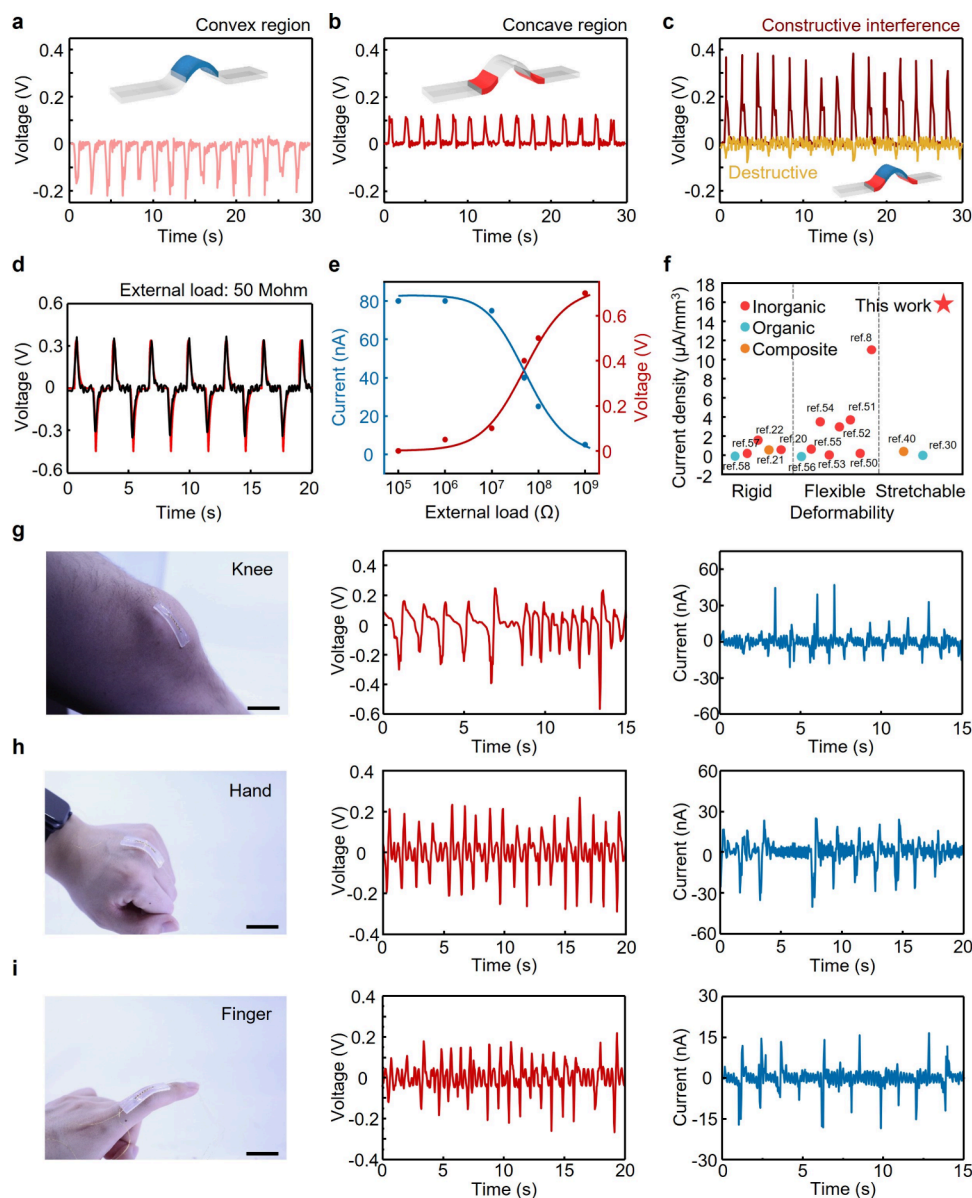


Figure 3. Validation of the S-PENG. (a, b) Open-circuit voltages of the convex (blue) and concave (red) regions. (c) Voltage measured between electrodes with conventional (yellow) and curvature-specific design (red). (d) Experimental and analytical output voltages of the S-PENG, measured with external loads of 50 Mohm. (e) Measured (dots) and theoretically calculated (solid line) voltage and current under different external resistances varying from 0.1 M Ω to 1 G Ω at 2 Hz. (f) Comparison of current density of the S-PENG from this work and other references as a function of deformability. Detailed information can be found in Table S1. (g–i) On-body evaluation of the S-PENG. Output voltage and current recordings from the S-PENG, attached to the knee (g), hand (h), and finger (i) in wearable applications, with an external load of 100 Mohm. Scale bars: 5 cm.

annealing process of the PZT and serves as a sacrificial layer subsequently. The SiO₂ upper layer acts as a protective barrier for the PZT during exposure to the Cr etchant used for separating the device from the silicon wafer. Next, Pt is deposited to create the bottom electrodes, chosen for their stability during the PZT annealing process and their ability to enhance the crystallinity of the PZT material. The PZT thin film has a nominal thickness of approximately 500 nm to ensure mechanical flexibility of the curved structure. The sputtered PZT layer is lifted off using prepatterned photoresist to minimize chemical damage, offering advantages over wet etching methods involving nitric acid (HNO₃) and hydrogen fluoride.

Following annealing of the PZT thin film layer at 650 °C (Figure S1), the top and interconnect metals are patterned, and the top side of the device is encapsulated with polyimide (PI). In the first transfer-printing step, a poly(dimethylsiloxane) (PDMS) stamp is utilized to transfer the device to the PI film by dissolving the sacrificial Cr layer. Anchoring sites are incorporated to hold the device before the pick-up process. Bonding sites to the elastomeric substrate are defined using patterned SiO₂ after the first transfer to PI. Figure 2b illustrates the top and bottom sides of the device after the first transfer-printing (Figure S2). The adhesive region is covered with SiO₂ to ensure local fixation of the device to the elastomeric substrate via siloxane bonding. The second transfer to the prestrained elastomeric substrate and the

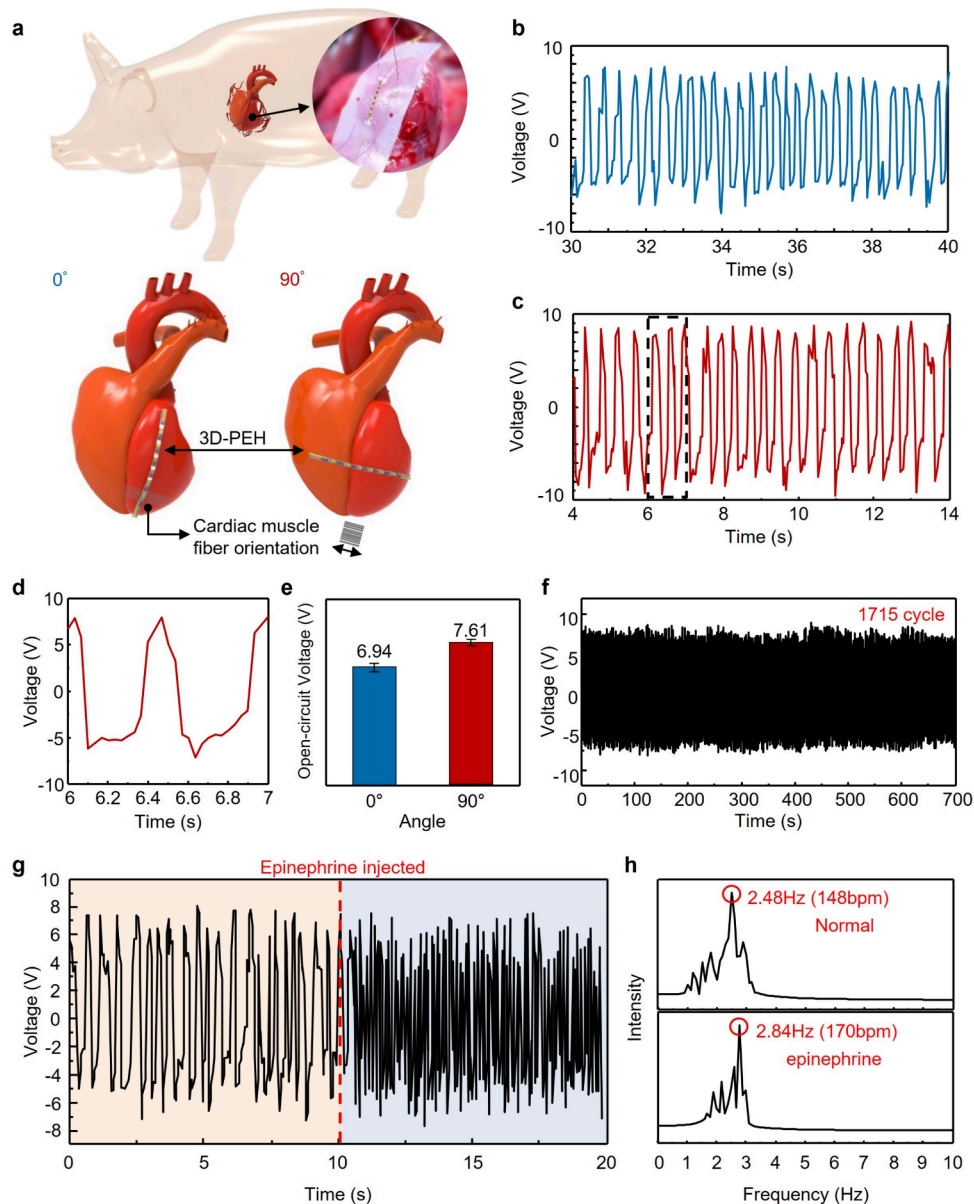


Figure 4. In vivo evaluation of the S-PENG. (a) Schematic illustration of a 30 kg porcine model and the attachment position of the S-PENG for biomedical applications. (b) Open-circuit voltage at an orientation of 0°. (c, d) Open-circuit voltage (c) and magnified views (d) at an orientation of 90°. (e) Maximum peak values of the open-circuit voltage measured at each orientation (0 and 90°). The error bar is the calculated standard error (95% confidence interval). (f) Mechanical stability of output voltage generated from the S-PENG. The output voltage increases in correlation with the bending strain induced by the porcine heart movement and maintains high stability over 1700 cycles. (g) Open-circuit voltages as a function of time, measured before and after epinephrine injection, and (h) corresponding heart rates, increasing from 148 to 170 bpm.

release of the prestrain complete the fabrication process. Poling was performed prior to compressive buckling in silicone oil at 150 °C with an applied voltage of 80 kV/mm. A temporary parallel connection circuit was constructed to match the direction of poling in vertical direction (Figure S3a,b). This temporary circuit configuration is replaced by serial interconnection after poling to maximize the efficiency of energy harvesting (Figure S3c,d).

Figure 2c,d depicts the images of the device attached to prestrained and sequentially released elastomeric substrates, respectively (Figure S4). The bottom images show the FEA results visualizing the local strain in the xx direction after the formation of compressive buckling, indicating opposite strain depending on the curvature. These local strains in opposite

directions enhance the dielectric polarization in the concave regions and weaken it in the convex regions, creating a voltage difference between these regions (Figure S3e–g). Figure 2e presents the images of uni- and biaxially stretchable PENGs with curvature-dependent coupling electrodes. The biaxially stretchable PENG can maximize energy harvesting from the 2D motion exhibited by the surface of human organs. Various design configurations can be explored to tailor the performance to the varying stretching scenarios.

Experimental Demonstration and On-Body Applications. To experimentally demonstrate the feasibility of utilizing stretchable PZT ribbons with curvature-specific coupling electrodes, the output of a single strap of the S-PENG was tested under various circumstances. The stretch-

ing/bending stage and the ribbons under test are depicted in Figure S5. Figure 3a,b illustrates the opposite signs of the change in the open-circuit voltages depending on the curvature (convex or concave). In the initial state without global strain, the PZT ribbons are in a 3D buckling shape, and there is no voltage difference between the top and bottom electrodes. As the PZT ribbons flatten with global strain, the regions return to their original polarization levels (poling), resulting in decreased polarization in concave regions and increased polarization in convex regions. During this process, the capacitive charges in the top and bottom electrodes remain mostly stationary in open circuit, leading to the concave region (blue) exhibiting a negative output voltage, while the convex region (red) shows a positive output voltage (Figures S6 and S7). Figure 3c shows the output voltage of the S-PENG depending on the circuit configuration (serial or parallel interconnection) (Figure S8). When the convex and concave regions are electrically interconnected in parallel, the equivalent circuit of the S-PENG is shown in Figure S8a and is equivalent to the circuit configuration of the S-PENG with conventional electrodes described in Figure 1b. Therefore, the voltage generated in each region cancels out, significantly reducing the energy harvesting efficiency. Conversely, when they are connected in series, the voltages generated in each region undergo constructive interference, resulting in an enhanced overall output voltage. The trends observed in the experimental data align with those predicted by theoretical analysis, lending credibility to the mechanisms of the curvature-specific coupling design.

Figure 3d and Figure S9 show the output voltages of the S-PENG, both experimentally measured and theoretically predicted (Supporting Note 1), with external loads of 10, 50, and 100 Mohm. The theoretically predicted voltage–time curve (eq S16) accurately conforms to the observed experimental data.

$$V_{\text{output}}(t) = \frac{4\bar{\epsilon}\pi t_{\text{pzt}}b_{\text{pzt}}(d_{\text{pzt}} - z_n)}{\bar{k}A_{\text{pzt}}W_{\text{in}}} e^{-2nR_{\text{int}}R_{\text{ext}}t_{\text{pzt}}/\bar{k}A_{\text{pzt}}(2nR_{\text{ext}}+R_{\text{int}})t} \int_0^t \frac{\partial(1 + \epsilon_{\text{pre}})A}{\partial t} e^{2nR_{\text{int}}R_{\text{ext}}t_{\text{pzt}}/\bar{k}A_{\text{pzt}}(2nR_{\text{ext}}+R_{\text{int}})t} dt$$

where $\bar{\epsilon}$ represents the effective piezoelectric constant and t_{pzt} , b_{pzt} , and A_{pzt} denote the thickness, width, and area of the PZT layer, respectively. d_{pzt} and z_n are the z -positions of the center of the PZT layer and the neutral plane, respectively. \bar{k} is the effective dielectric constant, W_{in} is the length of the buckling region, n represents the number of the periodic buckling structures, and R_{int} and R_{ext} are the internal resistance and external load, respectively. Further demonstrating a characteristic of the S-PENG, the switching polarity test showed polarity inversion when electrical lead-out connections are reversed (Figure S10), thus validating the piezoelectric effect of the S-PENG.

Figure 3e and Figure S11 illustrate the output characteristics of the S-PENG under varying external load resistances ranging from 0.1 M Ω to 1 G Ω . The measured voltage and current outputs (red and blue dots) align closely with the theoretical predictions (solid lines), showing an increase in the voltage and a corresponding decrease in the current as the resistance increases. The power density, derived from these measurements, peaked at approximately 8.34 mW/cm³ at 50 M Ω ,

demonstrating optimal performance under this condition. Peaks in the current signal (external load; 100 Mohm) were observed during moments of stretching and releasing. Based on these peaks, the current density of the S-PENG, calculated as 15.64 $\mu\text{A}/\text{mm}^3$, is comparatively higher than those of other reported PENGs (Figure 3f and Table S1).^{8,20–22,30,40,50–58} The volume used to calculate the current density is based on the effective area and the thickness of active materials. Additional measurements with the device wrapped around the curved surface of the body, such as knees, hands, and fingers, are shown in Figure 3g–i. The stretching and releasing motion of the body parts deform the attached device, generating peaks in output voltage.

Energy Harvesting in an Animal Model. In vivo evaluations were conducted to leverage biomechanical energy from cardiac motions. The S-PENG was implanted near the left ventricle (LV) of a porcine heart, as shown in Figure 4a and Figure S12. Following anesthesia, a median sternotomy was performed and the S-PENG was sutured onto the epicardium. The device, encapsulated in a polyimide film, effectively isolates the PZT from biofluids and tissues, similar to previous studies on implantable PENGs.^{8,52,53,59–62} This encapsulation mitigates the inherent cytotoxicity of PZT, ensuring biocompatibility of the device. The elastomeric substrate (Ecoflex-0030; thickness of 1 mm) adhered naturally to the epicardium and was secured at its four corners with sutures. To investigate the electrical output in relation to the implantation site, the device was attached to the LV area (0°) and across the direction between the LV and RV (90°) of the porcine heart, as illustrated in Figure 4a.

Figure 4b–d shows the open-circuit output voltages from the device mounted at the 0 and 90° mounting sites, with the averaged half the absolute value of the difference between the positive and negative peaks reaching 6.94 V at 0° and 7.61 V at 90° (Figure 4e). These results indicate that the device mounted at the 90° site generates an output voltage higher than that at the 0° site of the porcine heart. This enhanced output voltage at the 90° site not only underscores the significance of attachment location in optimizing energy harvest but also aligns with findings from previous studies. The device also consistently generates stable output voltages over 1700 cycles, as shown in Figure 4f. The buckling structure's adaptability to the heart's contraction and relaxation phases enhances the durability, contributing significantly to its effective energy harvesting.

To assess the S-PENG's performance under variable cardiac conditions, an experiment involving the administration of epinephrine was conducted to increase the heart rate. Before administration of epinephrine, the heart rate was 148 bpm, which increased to 170 bpm following the injection. Figure 4g illustrates the open-circuit output voltages, captured both before and after epinephrine administration. Corresponding to the rise in the heart rate, the voltage generation frequency increased. While the heart rate rise led to an increase in the voltage generation frequency, the magnitude of the output voltage showed no significant change due to the modest increase in the heart rate from epinephrine injection and the minimal impact of frequency on the open-circuit voltage measurement method (Figure S13). Additionally, converting the output voltage data into the frequency domain revealed that the peak intensity aligned with the heart rates measured pre- and postepinephrine injection (Figure 4h).

CONCLUSIONS

In this study, we introduced an approach to stretchable energy harvesting by developing a 3D buckling structure in PZT materials complemented by a curvature-specific coupling electrode design and an optimized circuit configuration. This approach has validated the feasibility of realizing an S-PENG with buckling structures, setting it apart from conventional PENG designs. Our proposed S-PENG design enables efficient electrical energy harvesting even when the buckling structure exhibits a geometrically distributed curvature with zero average. This design circumvents the typical cancellation of electrical output observed in conventional systems, ensuring that each segment of the nanogenerator effectively contributes to overall energy production. We confirmed the reliability of our design through theoretical and simulation analyses. Additionally, by demonstrating that the characteristics of the S-PENG predicted by simulations and theory align with experimental data, we have experimentally proven the feasibility of our design. This S-PENG achieves a maximum output of 8.34 mW/cm^3 at an optimal load resistance of $50 \text{ M}\Omega$. The practical applications of our technology were underscored through wearable applications and implantable *in vivo* experiments using a porcine heart. Our device has proven its capability to harvest energy from body movements when attached to various body parts (knee, hand, and finger). Moreover, we verified that it can successfully harvest energy from the surface of a porcine heart during repeated expansion and contraction. These experiments not only confirmed the mechanical and functional viability of our device but also showcased its potential as a PZT-based stretchable PENG, a task that was extremely challenging with conventional designs. Additionally, this strategy is versatile, as it is not limited by the type of piezoelectric material or strain-insensitive structure. While we used PZT as the piezoelectric material in this study, our strategy remains theoretically valid for other materials, such as PVDF or composite-based piezoelectric materials. Furthermore, as long as the distribution of local strain can be accurately predicted, efficient electrode and circuit designs can be achieved by using our method with various strain-insensitive structures, such as woven, serpentine, helical, and kirigami structures. Although our strategy theoretically offers broad applicability, further experimental validation and further future studies are required to fully explore and confirm its effectiveness. In conclusion, our study represents a significant breakthrough in piezoelectric energy harvesting technology. By overcoming the limitations of conventional S-PENGs systems, we have opened possibilities for the development of stretchable, efficient, and robust S-PENGs.

METHODS

Fabrication of the 2D Precursor for the Piezoelectric PENG.

The process began with the deposition of a Cr sacrificial layer on silicon wafers, followed by the deposition of a SiO_2 barrier layer on top of the Cr layer. The bottom electrode was formed using Pt/Ti layers (100 nm/10 nm in thickness), deposited via electron beam evaporation, and then defined through a lift-off process (AZ 5214E, MicroChem). A PZT film (500 nm in thickness) was deposited through sputtering and then patterned using a double-layer lift-off method (LOR 5B and AZ 4620, MicroChem). The annealing process was performed in a conventional furnace at $650 \text{ }^\circ\text{C}$ for 1.5 h. The Au/Cr layer (50 nm/5 nm in thickness) was patterned as the top electrode using a lift-off process, followed by a coating of polyimide. To connect the top electrode to the interconnect layer, a via hole was created by using photolithography and dry etching via reactive ion

etching. Next, the interconnect layer, composed of Au/Cr (50/5 nm in thickness), was deposited via sputtering and subsequently patterned using a wet etching process. Polyimide was then applied for encapsulation, patterned using photoresist, and dry etched via reactive ion etching. Subsequently, the SiO_2 barrier layer was also dry etched by using reactive ion etching. To form a bottom polyimide layer, which acts as the bottom encapsulation and controls the neutral plane, photoresist anchoring and Cr sacrificial layer removal processes were applied to the 2D precursor. The temporary substrate, consisting of a silicon wafer layered with PMMA and topped with a cured polyimide layer, was further coated with an uncured thin polyimide layer (6000 rpm, 30 s). The 2D precursor was then picked up using a PDMS stamp with a 1:4 ratio (Sylgard 184, Dow Corning) and transfer-printed onto the temporary substrate. During the transfer printing process, the 2D precursor was attached to the temporary substrate and then heated on a hot plate at $110 \text{ }^\circ\text{C}$ for 10 min. Any photoresist residue was removed from the 2D precursor, and it was cured on a hot plate at $150 \text{ }^\circ\text{C}$ for 10 min. Afterward, a final encapsulation layer of polyimide was coated and cured in a vacuum oven at $250 \text{ }^\circ\text{C}$ for 2 h. The device configuration and the via holes for the contact pads were defined using photolithography and dry etched via reactive ion etching.

Preparation of the S-PENG. Transfer of the 2D precursor onto the elastomeric substrate began with the removal of the PMMA sacrificial layer by using acetone. Next, the 2D precursor was picked up with a PDMS stamp, and a shadow mask was attached to define the bonding site. The bonding layer of SiO_2/Ti (50/10 nm in thickness) was deposited via sputtering, and the shadow mask was then removed from the device. The elastomeric substrate (Ecoflex 00-30, Smooth-On) was stretched by using a custom mechanical stretcher. Subsequently, the substrate was exposed to ultraviolet-induced ozone for 5 min to chemically functionalize it for bonding. The 2D precursor was attached onto the elastomeric substrate and heated at $70 \text{ }^\circ\text{C}$ for 20 min to achieve siloxane bonding. After removing the PDMS stamp and releasing the prestrain, the 3D PZT device was completed.

Poling and Measurement of Piezoelectric Characteristics.

The PZT thin film at the end step of the 2D precursor fabrication was poled at 80 kV/cm of electric field at $150 \text{ }^\circ\text{C}$ for 2 h. The electrical data acquisition equipment included a 6514 electrometer (Keithley), a bending machine system (SNM), a DMA 850 (TA Instruments), and a LabVIEW interface. The electrometer with the LabVIEW system measured open-circuit voltage and short-circuit current. The bending machine and DMA system produced linear motions of the device.

In Vivo Study. The study protocol was approved by the Korea Research Institute of Bioscience & Biotechnology – IACUC (approved number KRIBB-AEC-23108). A pig (male, 30 kg) was anesthetized by intramuscular injection of zolazepam and tiletamine (2.5 mg/kg), xylazine (3 mg/kg), and atropine (0.05 mg/kg). Inhalant anesthesia was maintained with isoflurane (1–2%) and oxygen (2 L/h) using an anesthesia machine (vaporizer + ventilator) and an endotracheal tube. After achieving adequate anesthesia, a median sternotomy was performed using standard surgical instruments. The S-PENG was sutured onto the epicardium with a stitch at each corner of the device. The S-PENG was connected to an electrometer (Keithley 6514) to measure the electrical output voltage from cardiac motion. Emergency and heart rate control drugs, including epinephrine and beta-blockers, were prepared and kept ready. An intravenous saline set was used to maintain hydration.

Simulation Analysis of the S-PENG. Software (COMSOL MULTIPHYSICS) was employed to numerically analyze the mechanical stability and electrical performance of the S-PENG. The structural mechanics module set up layered shell and linear elastic materials to study strain as a result of deformations in the S-PENG. Additionally, the AC/DC and circuit modules were used to analyze the electrical characteristics of the S-PENG, implementing a multiphysics setting (Piezoelectric materials) in the PZT domain to model the piezoelectric effect. All materials composing the S-PENG, except for PZT, were configured as isotropic materials, while PZT was

set as anisotropic. The properties of each material appear in Table S2. To implement the buckling structure of the S-PENG and increase computational convergence, a negligible vertical force (0.1 μN) was applied along a straight line at the center of each concave region. This force, considerably smaller than the device's flexural modulus, does not affect the results. The entire bottom electrode (Pt) was set to ground, and the circuit configuration was established as an open circuit. For accurate numerical analysis, a much denser mesh was formed around the center of concave regions and along the edges of convex regions.

ASSOCIATED CONTENT

Supporting Information

The Supporting Information is available free of charge at <https://pubs.acs.org/doi/10.1021/acsnano.4c09933>.

Supporting Note, Figure S1–S13, Tables S1–S2 and Supporting Movies S1–S3 are included in the Supporting Information. Supporting Information is available from the ACS Publications or from the author (PDF)

Videos of the compressive buckling process and mechanical stretching system (AVI, AVI)

AUTHOR INFORMATION

Corresponding Authors

Yoon Kyeong Lee – Department of Nano Convergence Engineering and Division of Advanced Materials Engineering, Jeonbuk National University, Jeonju 54896, Republic of Korea; Email: yoonklee@jbnu.ac.kr

Kyung-In Jang – Department of Robotics and Mechatronics Engineering, Daegu Gyeongbuk Institute of Science and Technology (DGIST), Daegu 42988, Republic of Korea; orcid.org/0009-0000-9126-2628; Email: kijang@dgist.ac.kr

Authors

Junwoo Yea – Department of Robotics and Mechatronics Engineering, Daegu Gyeongbuk Institute of Science and Technology (DGIST), Daegu 42988, Republic of Korea

Jeongdae Ha – Department of Robotics and Mechatronics Engineering, Daegu Gyeongbuk Institute of Science and Technology (DGIST), Daegu 42988, Republic of Korea

Kyung Seob Lim – Futuristic Animal Resource and Research Center, Korea Research Institute of Bioscience and Biotechnology (KRIBB), Cheongju 28116, Republic of Korea

Hyeokjun Lee – Department of Robotics and Mechatronics Engineering, Daegu Gyeongbuk Institute of Science and Technology (DGIST), Daegu 42988, Republic of Korea

Saehyuck Oh – Department of Robotics and Mechatronics Engineering, Daegu Gyeongbuk Institute of Science and Technology (DGIST), Daegu 42988, Republic of Korea

Janghwan Jekal – Department of Robotics and Mechatronics Engineering, Daegu Gyeongbuk Institute of Science and Technology (DGIST), Daegu 42988, Republic of Korea

Tae Sang Yu – Department of Robotics and Mechatronics Engineering, Daegu Gyeongbuk Institute of Science and Technology (DGIST), Daegu 42988, Republic of Korea

Han Hee Jung – Department of Information and Communication Engineering, Hannam University, Daejeon 34430, Republic of Korea

Jang-Ung Park – Department of Materials Science and Engineering, Yonsei University, Seoul 03722, Republic of Korea; orcid.org/0000-0003-1522-4958

Taeyoon Lee – Department of Electrical and Electronic Engineering, Yonsei University, Seoul 03722, Republic of Korea; orcid.org/0000-0002-8269-0257

Jaewoong Jeong – School of Electrical Engineering, Korea Advanced Institute of Science and Technology (KAIST), Daejeon 34141, Republic of Korea; orcid.org/0000-0001-7607-5453

Hoe Joon Kim – Department of Robotics and Mechatronics Engineering, Daegu Gyeongbuk Institute of Science and Technology (DGIST), Daegu 42988, Republic of Korea; orcid.org/0000-0003-1180-7830

Hohyun Keum – Industrial Transformation Technology Department, Korea Institute of Industrial Technology (KITECH), Cheonan 31056, Republic of Korea; orcid.org/0000-0002-7236-7683

Complete contact information is available at:

<https://pubs.acs.org/doi/10.1021/acsnano.4c09933>

Author Contributions

#J.Y. and J.H. contributed equally. The manuscript was written through contributions of all authors. All authors have given approval to the final version of the manuscript.

Notes

The authors declare no competing financial interest.

ACKNOWLEDGMENTS

This work was supported by the National Research Foundation of Korea (NRF) funded by Ministry of Science and ICT (24-KUJoint-03, RS-202400415347, 24-SENS-01, HR22C1832). This research was also supported by the NAVER Digital Bio Innovation Research Fund, funded by NAVER Corporation (Grant No. 3720230070).

REFERENCES

- (1) Shi, B.; Liu, Z.; Zheng, Q.; Meng, J.; Ouyang, H.; Zou, Y.; Jiang, D.; Qu, X.; Yu, M.; Zhao, L.; Fan, Y.; Wang, Z. L.; Li, Z. Body-integrated self-powered system for wearable and implantable applications. *ACS Nano* **2019**, *13* (5), 6017–6024.
- (2) Upendra, B.; Panigrahi, B.; Singh, K.; Sabareesh, G. Recent advancements in piezoelectric energy harvesting for implantable medical devices. *J. Intell. Mater. Syst. Struct.* **2024**, *35* (2), 129–155.
- (3) Yang, S. Y.; Sencadas, V.; You, S. S.; Jia, N. Z. X.; Srinivasan, S. S.; Huang, H. W.; Ahmed, A. E.; Liang, J. Y.; Traverso, G. Powering implantable and ingestible electronics. *Adv. Funct. Mater.* **2021**, *31* (44), No. 2009289.
- (4) Sheng, H.; Zhang, X.; Liang, J.; Shao, M.; Xie, E.; Yu, C.; Lan, W. Recent advances of energy solutions for implantable bioelectronics. *Adv. Healthcare Mater.* **2021**, *10* (17), No. 2100199.
- (5) Zhou, H.; Zhang, Y.; Qiu, Y.; Wu, H.; Qin, W.; Liao, Y.; Yu, Q.; Cheng, H. Stretchable piezoelectric energy harvesters and self-powered sensors for wearable and implantable devices. *Biosens. Bioelectron.* **2020**, *168*, No. 112569.
- (6) Jiang, D.; Shi, B.; Ouyang, H.; Fan, Y.; Wang, Z. L.; Li, Z. Emerging implantable energy harvesters and self-powered implantable medical electronics. *ACS Nano* **2020**, *14* (6), 6436–6448.
- (7) Gong, S.; Cheng, W. Toward soft skin-like wearable and implantable energy devices. *Adv. Energy Mater.* **2017**, *7* (23), No. 1700648.
- (8) Dagdeviren, C.; Yang, B. D.; Su, Y.; Tran, P. L.; Joe, P.; Anderson, E.; Xia, J.; Doraiswamy, V.; Dehdashti, B.; Feng, X.; Lu, B.; Poston, R.; Khalpey, Z.; Ghaffari, R.; Huang, Y.; Slepian, M. J.; Rogers, J. A. Conformal piezoelectric energy harvesting and storage from motions of the heart, lung, and diaphragm. *Proc. Natl. Acad. Sci. U. S. A.* **2014**, *111* (5), 1927–1932.

- (9) Li, Z.; Zhu, G.; Yang, R.; Wang, A. C.; Wang, Z. L. Muscle-driven in vivo nanogenerator. *Adv. Mater.* **2010**, *22* (23), 2534–2537.
- (10) Panda, S.; Hajra, S.; Mistewicz, K.; In-na, P.; Sahu, M.; Rajaitha, P. M.; Kim, H. J. Piezoelectric energy harvesting systems for biomedical applications. *Nano Energy* **2022**, *100*, No. 107514.
- (11) Li, T.; Lee, P. S. Piezoelectric energy harvesting technology: from materials, structures, to applications. *Small Struct.* **2022**, *3* (3), No. 2100128.
- (12) Elvin, N.; Elvin, A.; Choi, D. A self-powered damage detection sensor. *Journal of Strain Analysis for Engineering Design* **2003**, *38* (2), 115–124.
- (13) Park, G.; Rosing, T.; Todd, M. D.; Farrar, C. R.; Hodgkiss, W. Energy harvesting for structural health monitoring sensor networks. *Journal of Infrastructure Systems* **2008**, *14* (1), 64–79.
- (14) Le, M. Q.; Capsal, J.-F.; Lallart, M.; Hebrard, Y.; Van Der Ham, A.; Reffe, N.; Geynet, L.; Cottinet, P.-J. Review on energy harvesting for structural health monitoring in aeronautical applications. *Progress in Aerospace Sciences* **2015**, *79*, 147–157.
- (15) Xie, S.; Yan, H.; Qi, R. A Review of Polymer-Based Environment-Induced Nanogenerators: Power Generation Performance and Polymer Material Manipulations. *Polymers* **2024**, *16* (4), 555.
- (16) Song, Y.; Yang, C. H.; Hong, S. K.; Hwang, S. J.; Kim, J. H.; Choi, J. Y.; Ryu, S. K.; Sung, T. H. Road energy harvester designed as a macro-power source using the piezoelectric effect. *Int. J. Hydrogen Energy* **2016**, *41* (29), 12563–12568.
- (17) Orrego, S.; Shoole, K.; Ruas, A.; Doran, K.; Caggiano, B.; Mittal, R.; Kang, S. H. Harvesting ambient wind energy with an inverted piezoelectric flag. *Appl. Energy* **2017**, *194*, 212–222.
- (18) Taylor, G. W.; Burns, J. R.; Kammann, S.; Powers, W. B.; Welsh, T. R. The energy harvesting eel: a small subsurface ocean/river power generator. *IEEE journal of oceanic engineering* **2001**, *26* (4), 539–547.
- (19) Kim, S.; Johnson, T. J.; Clark, W. W. Harvesting energy from a cantilever piezoelectric beam. In *Smart Structures and Materials 2004: Damping and Isolation*; SPIE: 2004, Vol. 5386, pp 259–268.
- (20) Lee, T.-G.; Lee, H.-J.; Kim, S.-W.; Kim, D.-H.; Han, S. H.; Kang, H.-W.; Kang, C.-Y.; Nahm, S. Piezoelectric properties of Pb (Zr, Ti) O₃-Pb (Ni, Nb) O₃ ceramics and their application in energy harvesters. *J. Eur. Ceram. Soc.* **2017**, *37* (13), 3935–3942.
- (21) Yan, X.; Zheng, M.; Gao, X.; Li, L.; Rödel, J.; Zhu, M.; Hou, Y. Ultrahigh energy harvesting performance in lead-free piezocomposites with intragranular structure. *Acta Mater.* **2022**, *222*, No. 117450.
- (22) Yu, X.; Hou, Y.; Yang, Z.; Gao, X.; Zheng, M.; Zhu, M. Boosting output current density of piezoceramic energy harvesters using three-dimensional embedded electrodes. *Nano Energy* **2022**, *101*, No. 107598.
- (23) Khalatkar, A. M.; Gupta, V. K. Piezoelectric energy harvester for low engine vibrations. *J. Renewable Sustainable Energy* **2017**, *9* (2), No. 024701.
- (24) Wei, C.; Jing, X. A comprehensive review on vibration energy harvesting: Modelling and realization. *Renewable and Sustainable Energy Reviews* **2017**, *74*, 1–18.
- (25) Toprak, A.; Tigli, O. Piezoelectric energy harvesting: State-of-the-art and challenges. *Appl. Phys. Rev.* **2014**, *1* (3), No. 031104.
- (26) Pradeesh, E.; Udhayakumar, S.; Vasundhara, M.; Vivek, V. V. Vibration based piezoelectric energy harvesting-a review. In *IOP Conference Series: Materials Science and Engineering*; IOP Publishing: 2020, Vol. 995, p 012007.
- (27) Yang, Z.; Zhou, S.; Zu, J.; Inman, D. High-performance piezoelectric energy harvesters and their applications. *Joule* **2018**, *2* (4), 642–697.
- (28) Han, M.; Wang, H.; Yang, Y.; Liang, C.; Bai, W.; Yan, Z.; Li, H.; Xue, Y.; Wang, X.; Akar, B.; Zhao, H.; Luan, H.; Lim, J.; Kandela, I.; Ameer, G. A.; Zhang, Y.; Huang, Y.; Rogers, J. A. Three-dimensional piezoelectric polymer microsystems for vibrational energy harvesting, robotic interfaces and biomedical implants. *Nat. Electron.* **2019**, *2* (1), 26–35.
- (29) Sun, R.; Carreira, S. C.; Chen, Y.; Xiang, C.; Xu, L.; Zhang, B.; Chen, M.; Farrow, I.; Scarpa, F.; Rossiter, J. Stretchable piezoelectric sensing systems for self-powered and wireless health monitoring. *Adv. Mater. Technol.* **2019**, *4* (5), No. 1900100.
- (30) Song, S.; Yun, K.-S. Design and characterization of scalable woven piezoelectric energy harvester for wearable applications. *Smart Mater. Struct.* **2015**, *24* (4), No. 045008.
- (31) Ding, Y.; Duan, Y.; Huang, Y. Electrohydrodynamically printed, flexible energy harvester using in situ poled piezoelectric nanofibers. *Energy Technol.* **2015**, *3* (4), 351–358.
- (32) Yan, Z.; Pan, T.; Wang, D.; Li, J.; Jin, L.; Huang, L.; Jiang, J.; Qi, Z.; Zhang, H.; Gao, M.; Yang, W.; Lin, Y. Stretchable micromotion sensor with enhanced sensitivity using serpentine layout. *ACS Appl. Mater. Interfaces* **2019**, *11* (13), 12261–12271.
- (33) Feng, X.; Yang, B. D.; Liu, Y.; Wang, Y.; Dagdeviren, C.; Liu, Z.; Carlson, A.; Li, J.; Huang, Y.; Rogers, J. A. Stretchable ferroelectric nanoribbons with wavy configurations on elastomeric substrates. *ACS Nano* **2011**, *5* (4), 3326–3332.
- (34) Qi, Y.; Kim, J.; Nguyen, T. D.; Lisko, B.; Purohit, P. K.; McAlpine, M. C. Enhanced piezoelectricity and stretchability in energy harvesting devices fabricated from buckled PZT ribbons. *Nano Lett.* **2011**, *11* (3), 1331–1336.
- (35) Ma, T.; Wang, Y.; Tang, R.; Yu, H.; Jiang, H. Pre-patterned ZnO nanoribbons on soft substrates for stretchable energy harvesting applications. *J. Appl. Phys.* **2013**, *113* (20), 204503.
- (36) Kim, Y. G.; Hong, S.; Hwang, B.; Ahn, S. H.; Song, J. H. Improved performance of stretchable piezoelectric energy harvester based on stress rearrangement. *Sci. Rep.* **2022**, *12* (1), 19149.
- (37) Hu, N.; Chen, D.; Wang, D.; Huang, S.; Trase, I.; Grover, H. M.; Yu, X.; Zhang, J. X.; Chen, Z. Stretchable kirigami polyvinylidene difluoride thin films for energy harvesting: design, analysis, and performance. *Physical Review Applied* **2018**, *9* (2), No. 021002.
- (38) Vinogradov, A.; Holloway, F. Electro-mechanical properties of the piezoelectric polymer PVDF. *Ferroelectrics* **1999**, *226* (1), 169–181.
- (39) Habib, M.; Lantgios, I.; Hornbostel, K. A review of ceramic, polymer and composite piezoelectric materials. *J. Phys. D-Appl. Phys.* **2022**, *55* (42), No. 423002.
- (40) Zhou, X.; Parida, K.; Halevi, O.; Liu, Y.; Xiong, J.; Magdassi, S.; Lee, P. S. All 3D-printed stretchable piezoelectric nanogenerator with non-protruding kirigami structure. *Nano Energy* **2020**, *72*, No. 104676.
- (41) Kim, K.; Yun, K.-S. Stretchable power-generating sensor array in textile structure using piezoelectric functional threads with hemispherical dome structures. *Int. J. Precis. Eng. anuf.-Gr Technol.* **2019**, *6*, 699–710.
- (42) Uchino, K. Piezoelectric composite materials. In *Advanced Piezoelectric Materials*; Elsevier: 2017, pp 353–382.
- (43) Sukumaran, S.; Chatbouri, S.; Rouxel, D.; Tisserand, E.; Thiebaud, F.; Ben Zineb, T. Recent advances in flexible PVDF based piezoelectric polymer devices for energy harvesting applications. *J. Intell. Mater. Syst. Struct.* **2021**, *32* (7), 746–780.
- (44) Khang, D. Y.; Rogers, J. A.; Lee, H. H. Mechanical buckling: mechanics, metrology, and stretchable electronics. *Adv. Funct. Mater.* **2009**, *19* (10), 1526–1536.
- (45) Jiang, H.; Sun, Y.; Rogers, J. A.; Huang, Y. Post-buckling analysis for the precisely controlled buckling of thin film encapsulated by elastomeric substrates. *Int. J. Solids Struct.* **2008**, *45* (7–8), 2014–2023.
- (46) Jiang, H.; Khang, D.-Y.; Fei, H.; Kim, H.; Huang, Y.; Xiao, J.; Rogers, J. A. Finite width effect of thin-films buckling on compliant substrate: experimental and theoretical studies. *J. Mech. Phys. Solids* **2008**, *56* (8), 2585–2598.
- (47) Jiang, H.; Sun, Y.; Rogers, J. A.; Huang, Y. Mechanics of precisely controlled thin film buckling on elastomeric substrate. *Appl. Phys. Lett.* **2007**, *90* (13), 133119.
- (48) Xu, D.; Hu, Y.; Bu, X.; Chen, H.; Jia, H. Energy harvesting properties of the d 31 type piezoelectric cantilever harvester. *Journal of Electroceramics* **2023**, *51* (3), 221–229.

(49) Chen, J.; Nabulsi, N.; Wang, W.; Kim, J. Y.; Kwon, M.-K.; Ryou, J.-H. Output characteristics of thin-film flexible piezoelectric generators: A numerical and experimental investigation. *Appl. Energy* **2019**, *255*, No. 113856.

(50) Do, Y. H.; Jung, W. S.; Kang, M. G.; Kang, C. Y.; Yoon, S. J. Preparation on transparent flexible piezoelectric energy harvester based on PZT films by laser lift-off process. *Sens. Actuator A-Phys.* **2013**, *200*, 51–55.

(51) Seveno, R.; Carbajo, J.; Dufay, T.; Guiffard, B.; Thomas, J.-C. Flexible PET/Al/PZT/Al/PET multi-layered composite for low frequency energy harvesting. *J. Phys. D-Appl. Phys.* **2017**, *50* (16), No. 165502.

(52) An, J.; Park, H.; Jung, Y. H.; Min, S.; Kim, D. H.; Joe, D. J.; Lee, S. G.; Hyeon, D. Y.; Je, Y.; Seo, H. S.; Jeong, U.; Hong, S.; Hwang, G. T.; Joung, B.; Lee, K. J. In vivo flexible energy harvesting on porcine heart via highly-piezoelectric PIN–PMN–PT single crystal. *Nano Energy* **2024**, *121*, No. 109227.

(53) Kim, D. H.; Shin, H. J.; Lee, H.; Jeong, C. K.; Park, H.; Hwang, G.; Lee, H.; Joe, D. J.; Han, J. H.; Lee, S. H.; Kim, J.; Joung, B.; Lee, K. J. In vivo self-powered wireless transmission using biocompatible flexible energy harvesters. *Adv. Funct. Mater.* **2017**, *27* (25), No. 1700341.

(54) Park, K.-I.; Xu, S.; Liu, Y.; Hwang, G.-T.; Kang, S.-J. L.; Wang, Z. L.; Lee, K. J. Piezoelectric BaTiO₃ thin film nanogenerator on plastic substrates. *Nano Lett.* **2010**, *10* (12), 4939–4943.

(55) Wu, W.; Bai, S.; Yuan, M.; Qin, Y.; Wang, Z. L.; Jing, T. Lead zirconate titanate nanowire textile nanogenerator for wearable energy-harvesting and self-powered devices. *ACS Nano* **2012**, *6* (7), 6231–6235.

(56) Bae, J.; Song, J.; Jeong, W.; Nandanapalli, K. R.; Son, N.; Zulkifli, N. A. B.; Gwon, G.; Kim, M.; Yoo, S.; Lee, H.; Choi, H.; Lee, S.; Cheng, H.; Kim, C.; Jang, K. I.; Lee, S. Multi-deformable piezoelectric energy nano-generator with high conversion efficiency for subtle body movements. *Nano Energy* **2022**, *97*, No. 107223.

(57) Hu, Y.; Parida, K.; Zhang, H.; Wang, X.; Li, Y.; Zhou, X.; Morris, S. A.; Liew, W. H.; Wang, H.; Li, T.; Jiang, F.; Yang, M.; Alexe, M.; Du, Z.; Gan, C. L.; Yao, K.; Xu, B.; Lee, P. S.; Fan, H. J. Bond engineering of molecular ferroelectrics renders soft and high-performance piezoelectric energy harvesting materials. *Nat. Commun.* **2022**, *13* (1), 5607.

(58) Zhang, Z.; Li, X.; Peng, Z.; Yan, X.; Liu, S.; Hong, Y.; Shan, Y.; Xu, X.; Jin, L.; Liu, B.; Zhang, X.; Chai, Y.; Zhang, S.; Jen, A. K. Y.; Yang, Z. Active self-assembly of piezoelectric biomolecular films via synergistic nanoconfinement and in-situ poling. *Nat. Commun.* **2023**, *14* (1), 4094.

(59) Huang, X.; Qin, Q.; Wang, X.; Xiang, H.; Zheng, J.; Lu, Y.; Lv, C.; Wu, K.; Yan, L.; Wang, N.; Xia, C.; Wang, Z. L. Piezoelectric nanogenerator for highly sensitive and synchronous multi-stimuli sensing. *ACS Nano* **2021**, *15* (12), 19783–19792.

(60) Dagdeviren, C.; Shi, Y.; Joe, P.; Ghaffari, R.; Balooch, G.; Usgaonkar, K.; Gur, O.; Tran, P. L.; Crosby, J. R.; Meyer, M.; Su, Y.; Chad Webb, R.; Tedesco, A. S.; Slepian, M. J.; Huang, Y.; Rogers, J. A. Conformal piezoelectric systems for clinical and experimental characterization of soft tissue biomechanics. *Nat. Mater.* **2015**, *14* (7), 728–736.

(61) Dagdeviren, C.; Javid, F.; Joe, P.; von Erlach, T.; Bense, T.; Wei, Z.; Saxton, S.; Cleveland, C.; Booth, L.; McDonnell, S.; Collins, J.; Hayward, A.; Langer, R.; Traverso, G. Flexible piezoelectric devices for gastrointestinal motility sensing. *Nat. Biomed. Eng.* **2017**, *1* (10), 807–817.

(62) Yi, Z.; Xie, F.; Tian, Y.; Li, N.; Dong, X.; Ma, Y.; Huang, Y.; Hu, Y.; Xu, X.; Qu, D.; Lang, X.; Xu, Z.; Liu, J.; Zhang, H.; Yang, B. A battery-and leadless heart-worn pacemaker strategy. *Adv. Funct. Mater.* **2020**, *30* (25), No. 2000477.